Article

Bimetallic PtAu-Decorated SnO₂ Nanospheres Exhibiting Enhanced Gas Sensitivity for Ppb-Level Acetone Detection

Xiaofeng Zhu [1,2], Pei Cao [2], Peng Li [2], Yue Yu [2], Ruihua Guo [2,*], Yongzhen Li [2,*] and Hui Yang [1,*]

1 School of Materials Science and Engineering, Zhejiang University, Hangzhou 310027, China; zhuxiaofeng@bjast.ac.cn
2 Institute for Smart Ageing, Beijing Academy of Science and Technology, Beijing 100089, China; caopei2022@163.com (P.C.); lipeng2023@bjast.ac.cn (P.L.); yuyue@bjast.ac.cn (Y.Y.)
* Correspondence: guoruihua@bjast.ac.cn (R.G.); liyongzhen@bjast.ac.cn (Y.L.); yanghui@zju.edu.cn (H.Y.)

Abstract: Acetone is a biomarker found in the expired air of patients suffering from diabetes. Therefore, early and accurate detection of its concentration in the breath of such patients is extremely important. We prepared Tin(IV) oxide (SnO₂) nanospheres via hydrothermal treatment and then decorated them with bimetallic PtAu nanoparticles (NPs) employing the approach of in situ reduction. The topology, elemental composition, as well as crystal structure of the prepared materials were studied via field emission scanning electron microscopy, transmission electron microscopy, X-ray photoelectron spectroscopy, and X-ray diffraction. The findings revealed that bimetallic PtAu-decorated SnO₂ nanospheres (PtAu/SnO₂) were effectively synthesized as well as PtAu NPs evenly deposited onto the surface of the SnO₂ nanospheres. Pure SnO₂ nanospheres and PtAu/SnO₂ sensors were prepared, and their acetone gas sensitivity was explored. The findings demonstrated that in comparison to pristine SnO₂ nanosphere sensors, the sensors based on PtAu/SnO₂ displayed superior sensitivity to acetone of 0.166–100 ppm at 300 °C, providing a low theoretical limit of detection equal to 158 ppm. Moreover, the PtAu/SnO₂ sensors showed excellent gas response (R_a/R_g = 492.3 to 100 ppm), along with fast response and recovery (14 s/13 s to 10 ppm), good linearity of correlation, excellent repeatability, long-term stability, and satisfactory selectivity at 300 °C. This improved gas sensitivity was because of the electron sensitization of the Pt NPs, the chemical sensitization of the Au NPs, as well as the synergistic effects of bimetallic PtAu. The PtAu/SnO₂ sensors have considerable potential for the early diagnosis and screening of diabetes.

Keywords: PtAu bimetal; SnO₂ nanospheres; acetone; gas sensor

1. Introduction

Early diagnosis and screening of chronic diseases are important factors for improving cure rates. Concentration changes of volatile organic compounds (VOCs) in human exhalation are closely linked to certain diseases, and analyzing these VOCs is a non-invasive and convenient method [1]. Among different gas biomarkers, acetone is the key factor reflecting the progress of diabetes and/or therapeutic effect, and its concentration can be used as the basis to diagnose diabetes [2]. Therefore, the rapid and effective detection of acetone is highly desirable. According to clinical analyses, the level of acetone exhaled by healthy people is 300–900 ppb, whereas its level exhaled by diabetic patients exceeds 1.8 ppm [3,4]. Faced with extremely low target gas (TG) concentrations and complex background environments, stricter requirements are required to construct high-performance gas sensors, enabling the recognition of acetone in breath at ppb levels with improved selectivity. Chemiresistive-gas-sensor-based non-invasive respiratory diagnoses have become a promising technique for portable disease screening compared to other respiratory component detection technologies due to their superior sensitivity, good material designability, low cost, compact size, easy integration into sensor arrays, and low power consumption [5,6].

Gas sensors employing metal oxide semiconductors (MOSs) are more convenient to carry and operate and respond more rapidly compared to traditional methods [7,8]. The core component of gas sensors, the MOS, offers the benefits of low price, strong specificity, and a facile manufacturing process [9]. MOS materials have a considerably broad application prospect in non-invasive and rapid diagnosis fields. Among them, Tin(IV) oxide (SnO_2), a common n-type broad bandgap semiconductor (E_g = 3.6 eV at a temperature of 300 K), is extensively employed as a gas sensor material due to its excellent stability as well as improved conductivity [10,11]. However, gas sensors solely relying on SnO_2 display drawbacks including poor response, limited selectivity, and excessively high operating temperatures (To) [12]. Therefore, to improve its gas sensitivity, researchers have sought to modify SnO_2 using various strategies, including changing the crystal structure and morphology, decorating catalysts, constructing heterostructures, developing charge transfer hybrids, and incorporating molecular probing along with sieving effects [13–17]. Among these strategies, the use of functionalized nanocatalysts involving hybrid nanocomposites with synergistic effects as well as the introduction of significantly active catalysts for gas chemisorption demonstrates remarkably enhanced sensitivity and selective detection ability [13].

Bimetallic nanoparticles (NPs), a type of heterogeneous catalyst, exhibit dual properties related to their parent metal. By introducing guest metals, the activity, durability, and selectivity of the bimetallic NPs can be considerably adjusted and enhanced due to their reported synergistic effects. This unique advantage provides enormous possibilities for high-performance gas sensors. Researchers such as Li et al. [18] demonstrated that bimetallic PdAu functionalization on SnO_2 nanosheets achieved the highly sensitive detection of formaldehyde and acetone and exhibited excellent reusability, reliability, and strong resistance to humidity and corresponding biomarkers in the human exhaled air. Zhu et al. [19] prepared $PdPt/In_2O_3$ nanospheres featuring various Pt and Pd ratios, achieving prompt hydrogen detection at 400 ppb, as well as improved selectivity, repeatability, and prolonged stability. The enhanced gas sensitization was because of the synergistic effects of Pd and Pt. Luo et al. [20] developed a ZnO hollow nanocube decorated with PdRh, which had a hollow framework rich in Rh and a Pd-rich core frame. The results of the study revealed that it exhibited improved H_2S-sensing properties. These enhancements were credited to the outstanding conductivity of its framework, which improved gas diffusion and specific surface area, the excellent catalytic capability of the PdRh bimetal, as well as the establishment of Schottky barrier-type junctions and defects. Feng et al. [21] synthesized AgPt-decorated WO_3 NPs that exhibited a significantly enhanced response towards acetone. This was because of the electronic as well as the chemical sensitization of the Pt and Ag NPs to the WO_3 NPs that enhanced the adsorption of oxygen and improved the reaction rate, thereby promoting the gas-sensing response. Therefore, the preparation of SnO_2 with a unique structure followed by functionalization with bimetallic NPs on the surface emerges as a significant strategy for producing sensing materials characterized by enhanced response levels and rapid response and recovery times, ideal for determining trace-level concentrations of acetone.

This study presents the fabrication of bimetallic PtAu-modified ($PtAu/SnO_2$) SnO_2 nanospheres while employing the simple and versatile approaches of hydrothermal [22,23] and in situ reduction. The structure as well as morphology of the SnO_2 nanospheres before and after the modification were examined through SEM, TEM, XRD, and XPS. Furthermore, the gas-sensitive-sensing efficiency of the obtained materials was explored by employing acetone as the analyte. The novelty of this study is evident in these two key elements: a simple fabrication approach along with outstanding gas detection efficiency. We prepared SnO_2 nanospheres by the hydrothermal method with tin tetrachloride ($SnCl_4$) as the precursor followed by decorating them with PtAu NPs on the SnO_2 surface through the in situ reduction of chloroplatinic acid (H_2PtCl_6) and chloroauric acid ($HAuCl_4$) employing ascorbic acid. The approach is considerably simple as well as efficient and does not introduce any surfactant. $PtAu/SnO_2$ displayed enhanced selectivity, sensitivity, and rapid

response and recovery times for acetone gas at the optimal response temperature (300 °C). The enhanced sensitivity was because of the electronic and chemical sensitization, as well as the synergistic effect of bimetallic PtAu. In addition, the ppb-level determination of acetone in breath was important to diagnose diabetes. In conclusion, the mechanism of gas detection in PtAu/SnO$_2$ nanospheres was deliberated.

2. Experimental Section

2.1. Materials and Precursors

SnCl$_4$ (99%), sucrose (99.5%), H$_2$PtCl$_6$ (8 wt.% in H$_2$O), HAuCl$_4$ (98%, Au 47.8%), as well as ascorbic acid ($\geq$99.0%) were supplied by Anhui Zesheng Technology Co., Ltd., Anqing, China. All the reactants employed for the synthesis were of analytical grade and were utilized as provided without any purification. Distilled (DI) water was employed during the entire study.

2.2. Preparation of SnO$_2$ Nanospheres

SnO$_2$ nanospheres were prepared via a straightforward one-step hydrothermal technique followed by calcination treatment. In a typical synthetic strategy, SnO$_2$ nanospheres were fabricated by dissolving 1.5 mmol of SnCl$_4$ in DI water (15 mL) while continuously being stirred, followed by the addition of 3 mmol sucrose. Following that, the prepared solution was moved to a 50 mL stainless steel autoclave lined with Teflon and kept at 180 °C (12 h). The precipitate was then left to cool to room temperature (RT) followed by centrifuging and washing multiple times with ethanol and DI water. Finally, the SnO$_2$ samples underwent drying at a temperature of 80 °C (6 h), followed by calcination in air for 4h at a temperature of 500 °C.

2.3. Synthesis of PtAu/SnO$_2$ Nanospheres

Figure 1 illustrates the synthesis of SnO$_2$ nanospheres decorated with bimetallic PtAu (PtAu/SnO$_2$). PtAu/SnO$_2$ decoration was carried out through the in situ reduction of H$_2$PtCl$_6$ along with HAuCl$_4$ employing ascorbic acid acting as the reduction agent. The fabrication was carried out by dispersing 0.1 g of SnO$_2$ nanospheres in DI water (10 mL) and ultrasound-treated (10 min). Following that, 130 μL HAuCl$_4$ (20 mM) and 230 μL H$_2$PtCl$_6$ (20 mM) were introduced to the obtained mixture. Following a brief interval, 1 mL of ascorbic acid solution with a molarity of 0.1 M was introduced to the mixture followed by stirring (4 h) at RT conditions. At last, the products (PtAu/SnO$_2$) were centrifuged and underwent washing using DI water followed by drying at 60 °C. Similarly, the fabrication of Au/SnO$_2$ and Pt/SnO$_2$ was carried out for comparison employing 130 μL HAuCl$_4$ (20 mM) and 230 μL H$_2$PtCl$_6$ (20 mM), respectively.
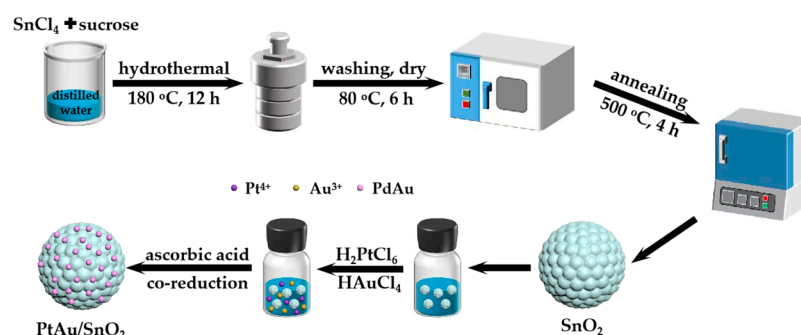

Figure 1. Fabrication of SnO$_2$ nanospheres decorated with PtAu NPs.

2.4. Material Characterization

Powder XRD (D/MAX-2600; Rigaku, Tokyo, Japan) was performed through a Cu-Kα radiation source (λ = 1.54056 Å, 150 mA, 40 kV) within the range spanning from 10° to 80°. The prepared samples were studied using a field emission scanning electron

microscope (FE-SEM, TESCAN MIRA LMS, TESCAN, Brno, Czech Republic) coupled with an energy-dispersive X-ray spectroscope at 15 kV, as well as an energy-dispersive X-ray (EDX) spectroscope. The TEM and the high-resolution transmission electron microscopy (HRTEM) images (JEM-F200, JEOL, Tokyo, Japan) were acquired through an accelerating voltage of 200 kV. XPS (K-Alpha, Thermo Scientific, Waltham, MA, USA) studies were carried out employing an Al Kα radiation source (1486.6 eV, 50 eV pass energy, 400 μm spot size), and all measured binding energies (BEs) corresponded with the C 1s peak found at 284.6 eV of surface indefinite carbon. Spectra were analyzed using Avantage 5.9931 software (Thermo Scientific). An inductively coupled plasma mass spectrometer (ICP-MS) (Agilent 7800, Santa Clara, CA, USA) was also employed for characterizing the samples. The working parameters of ICP-MS are detailed in Table S1.

2.5. Gas Sensitivity Experiments

The gas sensor was prepared as a side-heated structure. First, the prepared materials underwent grounding with a dispersant (DI water) within an agate mortar to produce a paste. The prepared paste was then applied employing a brush onto a ceramic tube (CT) upon which Pt-conducting wires and a couple of Au electrodes had been previously printed. The modified CT was dried at 180 °C for approximately 24 h to eliminate the DI water followed by welding onto a pedestal. Heating wires made of Ni–Cr were then pushed into the CT. The resulting sensors underwent aging at 300 °C (3 days) to enhance the mechanical strength and stability of the sensitive films.

A WS-30B gas sensor system from ZhengZhou Winsen Technology Co., Ltd., Zhengzhou, China. was employed to analyze the overall efficiency of the prepared gas sensor. The optimal temperature was determined by applying different heating voltages. Gas characteristics were assessed employing a stationary state gas distribution approach, wherein a standard gas was introduced inside a sealed chamber (18 L). The response of the gas sensor in this work was characterized using the ratio of the sensor resistance in various gas conditions as $S = R_a/R_g$; here, R_g and R_a denote the resistances of TG and the sensor in air, respectively. The RT relative humidity (RH) of the air was approximately 20%. The response time was specified as the duration required for the sensor to achieve 90% of the overall resistance change from its primary resistance. Conversely, the recovery time was the reverse. The amount of TG acquired from acetone was calculated using Equation (1) [24]:

$$V_x = \frac{V \times C \times M}{22.4 \times d \times p} \times 10^{-9} \times \frac{273 + T_r}{273 + T_b} \qquad (1)$$

where V_x (μL) is the liquid volume, V (mL) is the testing chamber volume, M (g) denotes the liquid molecular weight, C (ppm) is the liquid–vapor concentration, d (g/cm^3) is the liquid specific gravity, T_b (°C) is the test chamber temperature, T_r (°C) is the room temperature, and p is the purity of the liquid.

3. Results and Discussion

3.1. Material Characterisation

The crystal phases of the pure SnO_2 nanospheres and $PtAu/SnO_2$ nanospheres were analyzed by XRD. It is evident from Figure 2 that all the samples displayed intense diffraction signals and displayed Bragg reflections of the SnO_2 rutile structure (tetragonal) (110), (101), (200), (111), (210), (211), (220), (002), (310), (112), (301), (202), and (321) planes (JCPDS card no. 41-1445) [25]. No obvious peaks of the metallic NPs (Pt or Au) were found in the $PtAu/SnO_2$ nanospheres sample as the limit of detection was not sufficient for the identifying traces of Au and Pt NPs. On the other hand, the presence of Au and Pt was demonstrated by EDX and XPS (see below). The actual Pt and Au content in the $PtAu/SnO_2$ nanospheres determined by ICP-MS were 1.39 and 0.43 wt%, respectively.
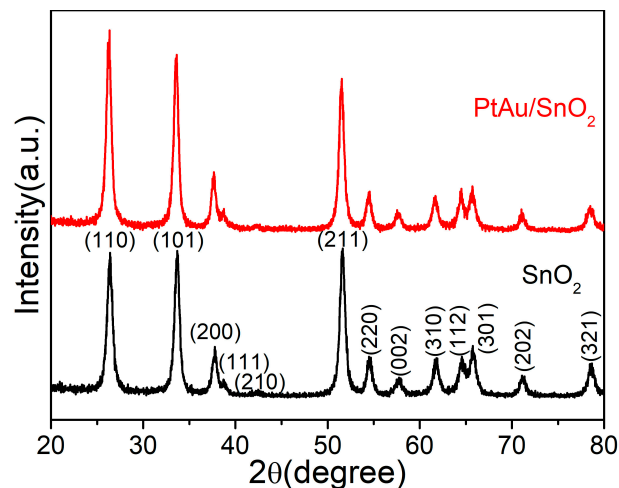
Figure 2. The obtained XRD spectra for the SnO_2 and $PtAu/SnO_2$ nanospheres.

The topologies of the pristine SnO_2 nanospheres and $PtAu/SnO_2$ nanospheres were characterized by FE-SEM. As depicted in Figure 3a,b, SnO_2 was composed of many accumulative rather than monodispersed nanospheres with diameters of approximately 500 nm. The surface of each individual sphere displayed roughness and comprised densely packed NPs. Elemental analysis by EDX mapping (Figure 3c–f) authenticated the presence of Au, Pt, O, and Sn, traced back to the SnO_2 nanospheres, while Au and Pt were attributed to the PtAu NPs. In addition, as shown in Figure 3e,f, Pt and Au, respectively, were uniformly distributed on the SnO_2 nanosphere surface.
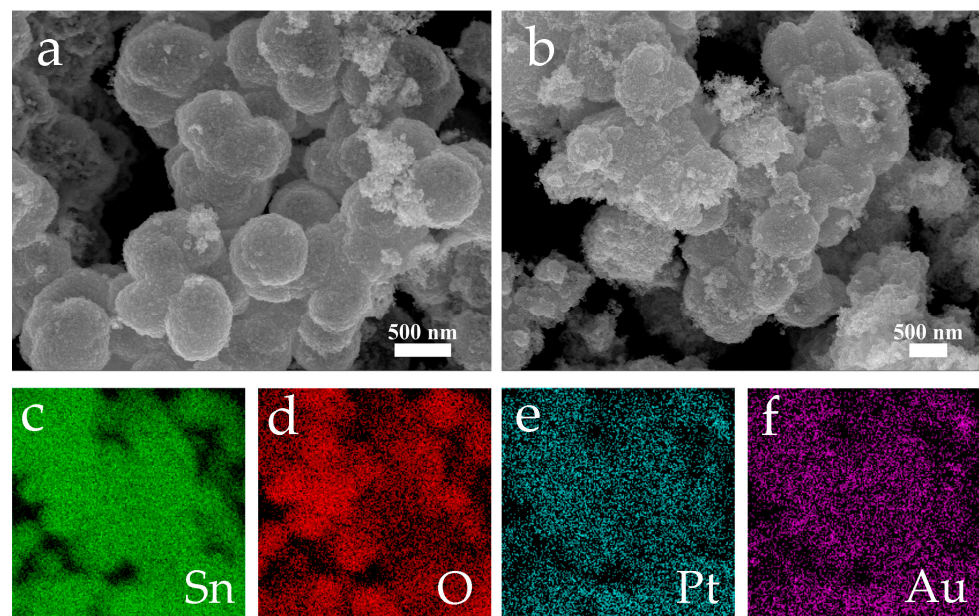

Figure 3. The acquired FE-SEM images for (**a**) the pristine SnO_2 nanospheres, (**b**) the $PtAu/SnO_2$, and (**c**–**f**) the FE-SEM elemental mapping images of (**b**).

The microstructure of the functionalized $PtAu/SnO_2$ nanospheres was determined by HRTEM. The selected area electron diffraction (SAED) pattern as well as the typical HRTEM lattice image of the $PtAu/SnO_2$ are shown in Figure 4. The HRTEM micrograph displayed in Figure 4a shows that the SnO_2 nanospheres were a single crystal structure with interplanar spacings equal to 0.335 and 0.264 nm, as determined from the lattice fringes that corresponded to the (110) and (101) SnO_2 rutile structure planes [11]. Furthermore, the characteristic interplanar 0.235 nm spacings correspond to the PtAu (111) planes, suggesting

the particle's structure comprised multiple crystals of both Au and Pt [25,26]. Additionally, the diffraction rings observed in the SAED patterns displayed in Figure 4b were ascribed to the planar directions of (110), (101), (211), and (111), indicating the tetragonal rutile structure of the SnO_2 crystallites and PtAu NPs.
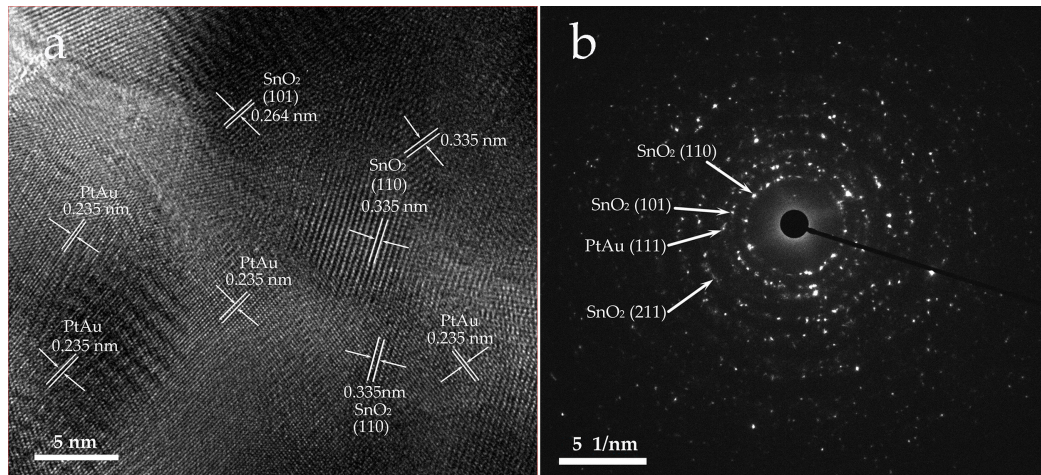

Figure 4. (**a**) The obtained HRTEM image for $PtAu/SnO_2$ and (**b**) SAED pattern of the $PtAu/SnO_2$.

The bonding state and chemical position of the Pt- and Au-loaded SnO_2 nanospheres were explored through XPS (Figure 5). The survey spectrums for pristine SnO_2 and $PtAu/SnO_2$ are displayed in Figure 5a, confirming the existence of Pt as well as Au in the $PtAu/SnO_2$ nanospheres. The high-resolution (HR) XPS analysis of Sn 3d in the pure SnO_2, Pt/SnO_2, Au/SnO_2, and $PtAu/SnO_2$ samples is presented in Figure 5b. All materials demonstrated two symmetrical signals, with the BE values derived from Sn $3d_{5/2}$ and Sn $3d_{3/2}$ [11,18]. Compared to pristine SnO_2, because of the incorporation of Au and Pt NPs on the nanosphere surface, the Sn 3d band of the Pt/SnO_2 and $PtAu/SnO_2$ samples moved towards lower BE values, while the Sn 3d signal of the Au/SnO_2 material shifted towards a higher value of BE. The displacement of the Sn 3d signal was because of the interface of SnO_2 with the Au as well as Pt NPs, resulting in the change in the electronic structure of the SnO_2 surface, thereby enhancing the detecting performance. Figure 5c shows the HR-XPS analysis of O 1s in the pure SnO_2, $PtAu/SnO_2$, Au/SnO_2, and Pt/SnO_2 samples. The O 1s XPS spectrum was resolved into three BE values at 530.45−530.78 eV, 531.12−531.78 eV, and 532.33−532.63 eV, which were associated with lattice oxygen (O_{lat}), defect oxygen (O_{def}), and adsorbed oxygen (O_{ads}), respectively [10]. It is generally believed that the surface O_{ads} ions would facilitate the adsorption process of gas sensing. It was found that the content of O_{ads} in $PtAu/SnO_2$ was higher than that of pure SnO_2, Pt/SnO_2, and Au/SnO_2, indicating that the loading of PtAu NPs could activate and dissociate O_2 in the ambient air and increase the content of O_{ads}, which would participate in the oxidation−reduction reaction, resulting in a larger change in the resistance of $PtAu/SnO_2$. The XPS peaks of Pt 4f were found in the obtained samples of Pt/SnO_2 and $PtAu/SnO_2$, as shown in Figure 5d, which were associated with Pt $4f_{7/2}$ and Pt $4f_{5/2}$. Similarly, the XPS peaks of Au 4f appeared in the obtained samples of Au/SnO_2 and $PtAu/SnO_2$, as shown in Figure 5e, which were attributed to Au $4f_{5/2}$. Compared to Pt/SnO_2 and Au/SnO_2, the XPS signals of Pt 4f and Au 4f observed in the $PtAu/SnO_2$ sample both moved towards lower BE values, further indicating the presence of a combined impact because of modification in the electronic structure of the PtAu NPs.
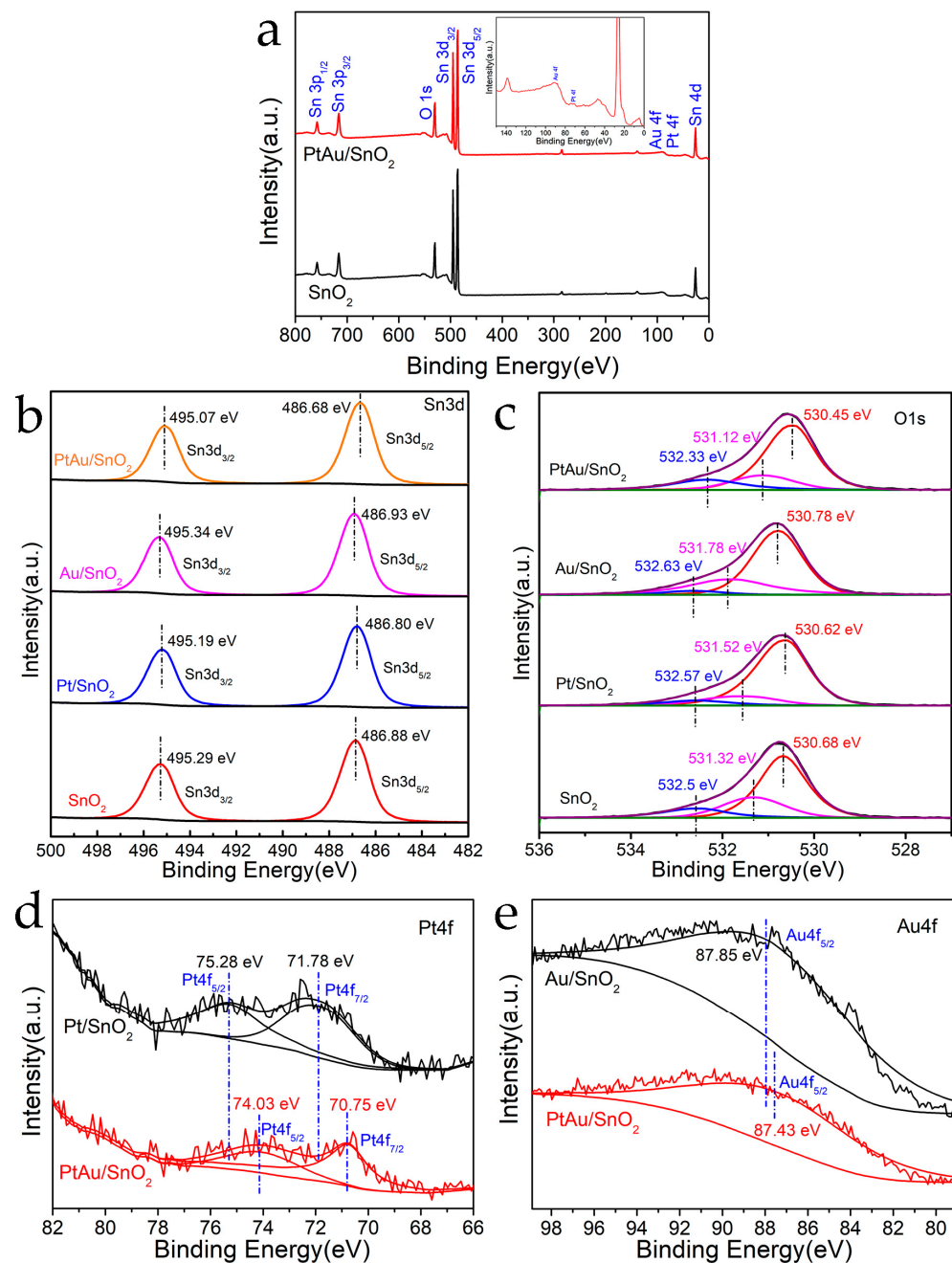
Figure 5. The obtained XPS survey spectrum for (**a**) pristine SnO_2 and $PtAu/SnO_2$, (**b**) Sn 3d, (**c**) O 1s, (**d**) Pt 4f, and (**e**) Au 4f HR-XPS spectrum for pristine SnO_2, Pt/SnO_2, Au/SnO_2, and $PtAu/SnO_2$.

3.2. Gas-Sensing Performance

The gas-detecting efficiencies of the pure SnO_2 as well as the $PtAu/SnO_2$ sensors were analyzed and compared. First, the responses of SnO_2 along with the $PtAu/SnO_2$ sensors to acetone (100 ppm) gas were tested in a temperature window spanning from 100 °C to 400 °C to optimize the optimal value To for the sensors (see Figure 6a). The trend of the gas sensitivity response for the sensors first increased to the maximum value as the value of *T*o enhanced, and after that declined with further temperature increased (Figure 6a). As the adsorbed molecular oxygen present on the material surface was activated to produce further active O_2^- and O^- species, the response increased as the value of To improved. This effect was observed consistently until the optimum To value was reached. Thereafter, the reaction decreased due to the significant desorption of reactants like reactive oxygen species (ROS) as well as the TG molecules. Given its volatility, the steady-state water of

the adsorbed acetone molecules slowly decreased as the temperature enhanced, which led to a lower sensor response. Therefore, the optimized value of To was the equilibrium point between two conflicting mechanisms. It is evident from Figure 6a that the optimized value of To for both the SnO_2 sensors and $PtAu/SnO_2$ sensors was 300 °C. The introduction of the PtAu NPs led to a reduction in the height of the energy hindrance along with an enhancement in activity at the surface, resulting in the much higher response of the $PtAu/SnO_2$ sensors to acetone (100 ppm) at 300 °C (R_a/R_g = 492.3) in comparison to the pristine SnO_2 sensors under the same conditions (R_a/R_g = 23.7). This was associated with the catalytic activity of the Au and Pt NPs, as well as the synergistic effect of the PtAu.
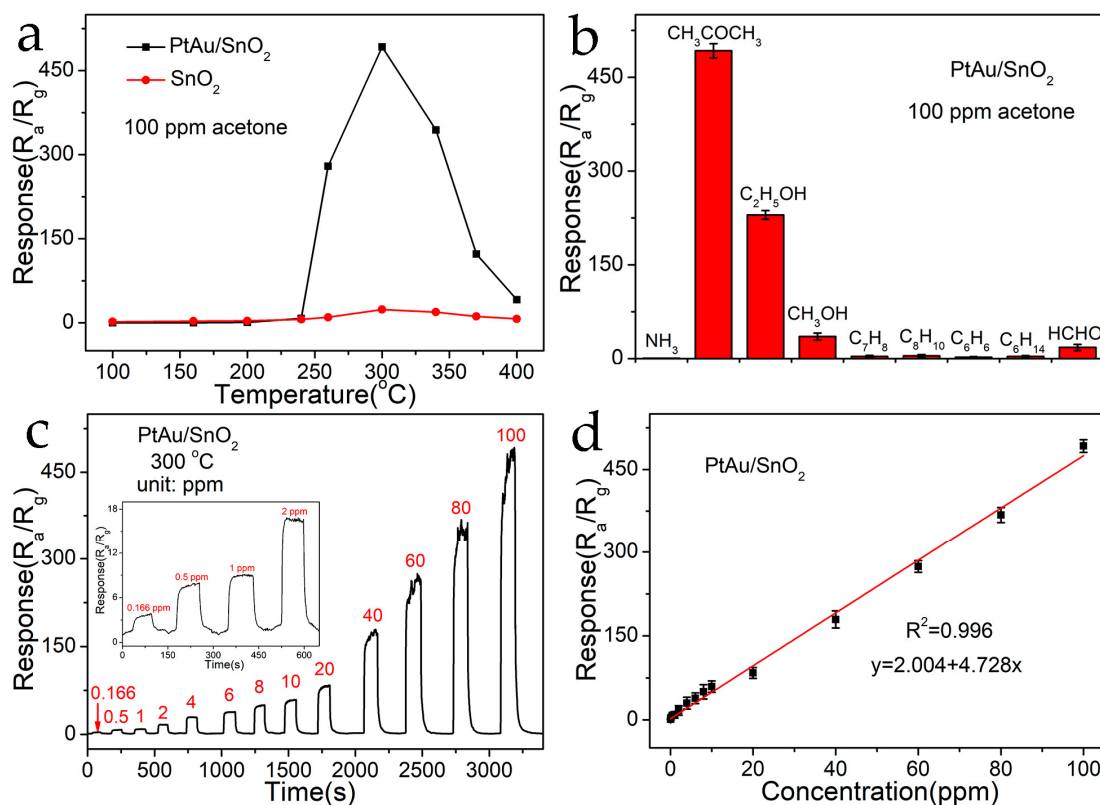

Figure 6. (**a**) Response of pristine SnO_2 sensors and $PtAu/SnO_2$ sensors to 100 ppm acetone at various temperature values. (**b**) Selectivity test of $PtAu/SnO_2$ sensors against 100 ppm of NH_3, CH_3COCH_3, C_2H_5OH, CH_3OH, C_7H_8, C_8H_{10}, C_6H_6, C_6H_{14}, and HCHO at 300 °C. (**c**) Dynamic response plots of $PtAu/SnO_2$ materials to varying amounts of acetone (0.166–100 ppm) at 300 °C. (**d**) Linear response of $PtAu/SnO_2$ sensors with acetone gas concentration.

Because the composition of gases exhaled by the human body is complex, it includes a variety of biomarkers. Therefore, the selectivity of the sensor holds importance. The selectivity of the $PtAu/SnO_2$ sensors to 100 ppm ammonia (NH_3), acetone (CH_3COCH_3), ethanol (C_2H_5OH), methanol (CH_3OH), toluene (C_7H_8), xylene (C_8H_{10}), benzene (C_6H_6), n-ethane (C_6H_{14}), and formaldehyde (HCHO) was studied at the optimal To value (300 °C) (Figure 6b). Among them, NH_3, C_2H_5OH, C_7H_8, as well as HCHO are typical biomarkers: NH_3 for kidney disease, C_2H_5OH for drunk driving, C_7H_8 for cancer, and HCHO for cardiovascular disease. As demonstrated in Figure 6b, the $PtAu/SnO_2$ sensors exhibited excellent selectivity for detecting acetone, exhibiting a response sensitivity (R_a/R_g) of 492.3, while the response sensitivities (R_a/R_g) for NH_3, C_2H_5OH, CH_3OH, C_7H_8, C_8H_{10}, C_6H_6, C_6H_{14}, and HCHO under the same conditions were 0.5, 229.8, 35.2, 3.5, 4.3, 2.1, 3.6, and 17.8, respectively.

Figure 6c shows the dynamic gas-sensitive performance of the $PtAu/SnO_2$ sensors to various concentrations of acetone (0.166–100 ppm) at the optimal To value of 300 °C.

The gas responses of the sensors improved as the acetone concentration improved, and the sensors could be employed for acetone determination across a long concentration range. The results also showed that the proposed sensor displayed an excellent linear correlation with the acetone concentration, with a linear correlation of 0.996 (Figure 6d). Even at trace concentrations of acetone gas, the sensor response was much higher than the measurement noise level. When the PtAu/SnO$_2$ sensors were exposed to 166 ppb acetone, the response value R_a/R_g was 3.9. Figure S1 displays the transient response plot of the PtAu/SnO$_2$ sensors to 166 ppb acetone at 300 °C. Using the relationship of detection limit (D_L) as given in Equations (S1) and (S2) for the PtAu/SnO$_2$ sensors [10], the D_L was 0.158 ppm (158 ppb) (see Supplementary Materials). The actual D_L was consistent with the result of the theoretical calculation. This concentration was well below the early diagnosis and monitoring of diabetes breath analysis concentration range: concentrations of acetone in the expired air from patients suffering from diabetes are >1.8 ppm in comparison to 300–900 ppb in the exhaled air from healthy people. Therefore, the PtAu-modified SnO$_2$ sensors are sensitive enough to detect the acetone biomarker associated with diabetes.

The response along with recovery times were characterized by the durations required for the prepared sensor to achieve 90% of its maximum response and recovery, respectively. These are the primary parameters for gas sensors; rapid and efficient response to TG is an essential characteristic of an outstanding sensor device. The response and recovery times of the PtAu/SnO$_2$ sensors to 10 ppm acetone at 300 °C were 14 s and 13 s, respectively (Figure 7a). The sensors revealed an excellent prompt response efficiency. The short time parameter of the PtAu/SnO$_2$ sensors was primarily because of the co-catalysis of PtAu, which accelerated the transfer of charge carriers as well as reduced the response and recovery times.
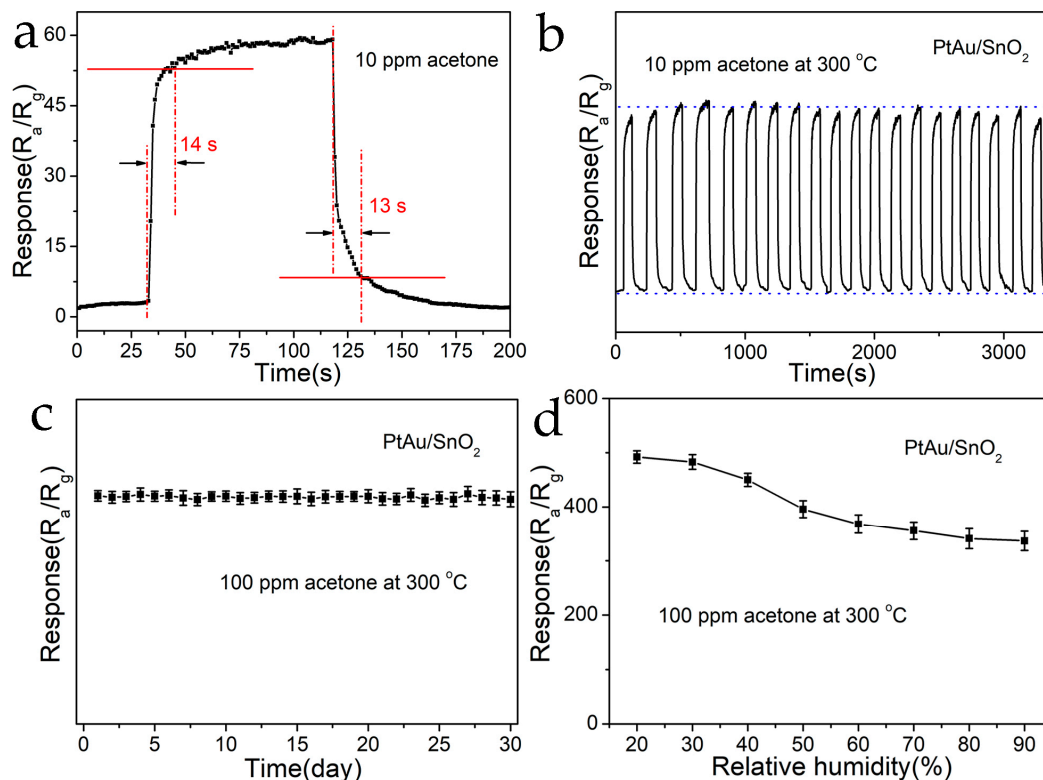

Figure 7. (**a**) The obtained response as well as recovery times for the PtAu/SnO$_2$ sensors to acetone (10 ppm) at 300 °C. (**b**) Repeatability of the PtAu/SnO$_2$ sensor to acetone (10 ppm) at 300 °C. (**c**) The 30-day stability tests of PtAu/SnO$_2$ sensors against acetone (10 ppm) at 300 °C. (**d**) Response of PtAu/SnO$_2$ sensor across varying relative humidities to acetone (100 ppm) at 300 °C.

The repeatability of the PtAu/SnO$_2$ sensors, required for their practical application, was explored. Figure 7b shows the repeatability curve of the PtAu/SnO$_2$ sensors in the presence of acetone (10 ppm) at 300 °C. The sensors underwent evaluation for 20 cycles, and the response values remained nearly consistent in every case, showing no significant variation. They also returned to their initial condition. This demonstrated that the prepared sensors exhibited good recovery and repeatability features. The prolonged stability of the PtAu/SnO$_2$ sensors, a further important aspect of their practical use, was also studied. As depicted in Figure 7c, the response of the developed sensor to acetone (100 ppm) at 300 °C was maintained at the original value after 30 days, and the vibration was small, which implied that the gas sensors exhibited good stability over long durations. The high repeatability along with good stability of the PtAu/SnO$_2$ sensors were associated with the structural stability of the SnO$_2$ nanospheres as well as co-promotion by the PtAu.

Humidity is another important parameter to consider in breath sensing. Figure 7d demonstrates the response curve of the PtAu/SnO$_2$ sensor to acetone (100 ppm) at 300 °C in different RH conditions. The results revealed a declining behavior as RH was enhanced in the range of 20–90%, which was possibly due to the reduced interaction between the PtAu/SnO$_2$ and acetone gas. Due to the enhanced humidity, additional water molecules got adsorbed onto the PtAu/SnO$_2$ surface, which made the chemisorption of oxygen and acetone molecules difficult and prevented the sensing reaction with acetone, thus resulting in decreased sensing performance [27]. When the value of RH reached 90%, the PtAu/SnO$_2$ sensor's response remained at 336.5 (~68.3% of the response at 20% RH), which indicated that the PtAu/SnO$_2$ sensors could be used for the detection of acetone at higher humidity.

Table 1 summarizes the comparison of the acetone-detecting characteristics of various gas-detecting materials. The proposed PtAu/SnO$_2$ sensors exhibited outstanding acetone gas detecting efficiency. In comparison to published approaches, our newly developed PtAu/SnO$_2$ sensor showed higher response values, quick response/recovery times, and low D$_L$. The current approach offered a significant strategy for enhancing acetone-sensing performance, particularly in improving response magnitude and reducing response/recovery time.

Table 1. A comparison of the acetone recognition efficiency achieved for different materials on the basis of published results and the current work. (Temp. = To, Conc. = acetone concentration, Res./Rec. Time = response/recovery time, D_L = detection limit).

Materials	Morphology	Temp. (°C)	Conc. (ppm)	Res.	Res./Rec. Time (s/s)	D_L (ppb)	Ref.
SnO$_2$	Nanosheets	280	1	10.4	40/610	200	[28]
ZnO/SnO$_2$	3D inverse opal photonic crystal balls	260	50	40.3	6/10	100	[6]
ZnO/SnO$_2$	Thick films	180	0.5	3.36	57/63	10	[29]
Co$_3$O$_4$/SnO$_2$	Yolk-shell nanofibers	350	100	217	0.62/46.5	100	[30]
Zn$_2$SnO$_4$/SnO$_2$	Hierarchical stack structure	275	30	33	13/66	64.25	[31]
Pt$_{40}$Cu$_{60}$/SnO$_2$	Octahedral alloy nanocrystal-decorated nanoclusters	240	5	22.04	1.5/58	20	[32]
PdAu/SnO$_2$	3D nanosheets	250	2	6.5	5/4	45	[18]
Au/WO$_3$-SnO$_2$	Corrugated nanofibers	150	0.5	79.6	—	—	[33]
Chitosan-Pt/SnO$_2$	Mesoporous nanofibers	350	1	38.4	12/44	5	[34]
PtAu/SnO$_2$	Nanospheres	300	10	59.4	14/13	158	Present study

3.3. Gas-Sensing Mechanisms

The sensing mechanism of SnO$_2$, a common n-type semiconductor material, follows the surface resistance control model (Figure 8), whereby the resistance variation of SnO$_2$ corresponds to the content as well as the type of chemisorbed oxygen (O$^-$, O$_2$$^-$ or O^{2-}) during the processes of desorption and adsorption [Equations (2)–(4)]. Typically, when

a SnO_2 sensor operates at an appropriate temperature and comes into contact with air, oxygen molecules adsorb onto its surface. These adsorbed molecules capture electrons from the conduction bands (CBs), forming chemically adsorbed oxygen ions and resulting in an enhanced SnO_2 resistance [9].
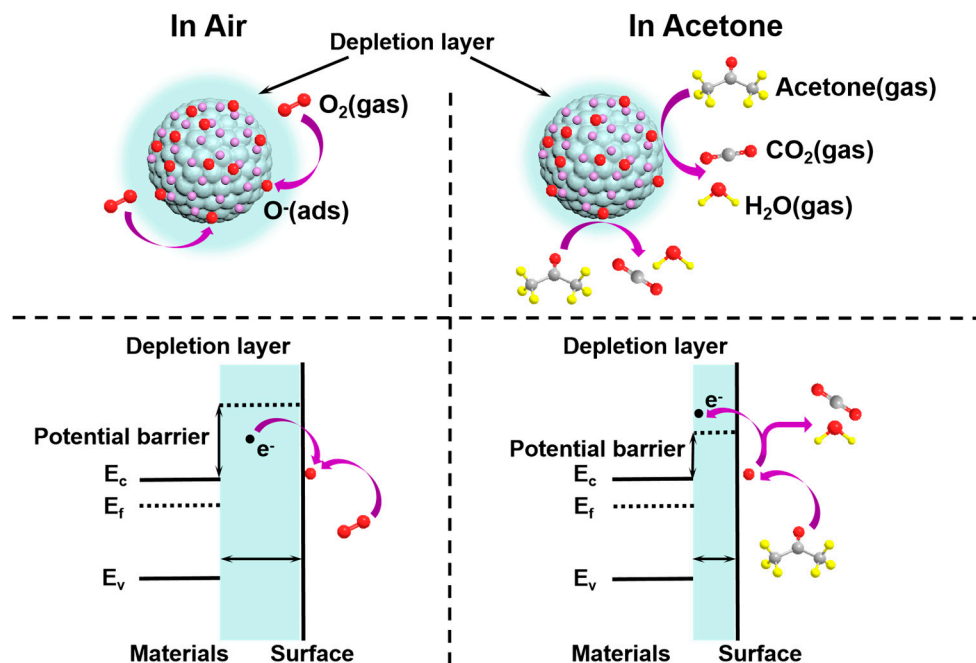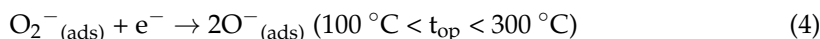
$$O_{2(gas)} \rightarrow O_{2(ads)} \tag{2}$$

$$O_{2(ads)} + e^- \rightarrow O_2{}^-{}_{(ads)} \ (t_{op} < 100\ ^\circ C) \tag{3}$$

$$O_2{}^-{}_{(ads)} + e^- \rightarrow 2O^-{}_{(ads)} \ (100\ ^\circ C < t_{op} < 300\ ^\circ C) \tag{4}$$

Figure 8. Gas-sensing mechanism of the $PtAu/SnO_2$ sensor. The upper images are schematic diagrams, and the bottom images are energy band diagrams.

When the SnO_2 sensor encounters a reducing gas, such as acetone, reactive oxygen ions interact with the TG, releasing electrons into the CBs of the SnO_2. This leads to a reduction in the resistance value of the SnO_2 sensor (Figure S2). In the current report, the surface reaction of the SnO_2 sensor is as follows [Equation (5)] [2]:

$$CH_3COCH_{3(gas)} + 8O^-{}_{(ads)} \rightarrow 3CO_{2(gas)} + 3H_2O_{(gas)} + 8e^- \tag{5}$$
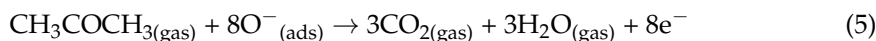
Here, it is evident that the sensor performance depends largely on the content of oxygen ion adsorption. Drawing from the findings of the gas detection characteristics, compared to the simple SnO_2 sensor, the addition of PtAu can improve the sensing performance of SnO_2 nanospheres for acetone 20.8 times. The catalytic effect of PtAu improves their sensitivity and selectivity to acetone. This catalytic effect comes from either electronic or chemical sensitization as follows [18,35]. First, Au and Pt NPs are recognized as chemical sensitizers with 'spillover impacts'. Pt and Au are superior oxygen dissociation catalysts compared to SnO_2. SnO_2 has a high availability for catalyzing the breakdown of molecular oxygen, resulting in the generation of ROS that spill over onto the surface of the metal oxides to produce further ROS. The high concentrations of chemically adsorbed O ions lead to a thicker layer where electrons are scarce, which leads to an increase in baseline resistance value within air. As noted in other literature, a thicker depletion zone enhances sensitivity. Therefore, the interaction between the measured acetone gas and chemically adsorbed O ions leads to a substantial change in the value of the resistance. Furthermore,

due to the high conductivity and abundance of free electrons in Pt and Au, the adsorption of O ions occurs onto the surface of metal NPs at reduced temperatures (including RT). This is believed to lead to a larger as well as rapid reaction between the determined gas molecules and the adsorbed O. The homogeneous distribution of small Au and Pt NPs on the SnO_2 nanosphere surface maximizes this impact. Second is the synergistic influence of bimetallic Pt/Au NPs. The synergistic effects in the current study can be interpreted by the following two aspects. First, the introduced PtAu NPs lead to changes in the electronic structure of the SnO_2 nanospheres at the surface and further activation of the lattice, demonstrated by the shift in the XPS BE band locations. Second, the combined catalytic effect of the PtAu NPs reduces the activation energy, thereby accelerating the reaction course between the acetone molecules and ROS through the uniform distribution of the nanocatalysts.

4. Conclusions

Bimetallic PtAu NP–NP-modified SnO_2 nanospheres were successfully synthesized using the one-step hydrothermal treatment and in situ reduction methods. The prepared $PtAu/SnO_2$ nanosphere sensor was applied to the gas-sensitive detection of acetone. Electron microscopy analysis indicated that uniform-sized PtAu NPs are dispersed on the surface of the SnO_2 nanospheres. The synthetic method was considerably simple and effective and did not introduce any surface activity. This approach can serve as a typical method for modifying bimetallic NPs on the surface of different MOS materials. The $PtAu/SnO_2$ nanosphere sensor exhibited a significantly enhanced gas-sensitive response, and it showed good selectivity and sensitivity (R_a/R_g = 492.3), fast response and recovery times (14 and 13 s, respectively), and an acetone gas D_L of 158 ppb at the optimal response temperature (300 °C). Compared to pure SnO_2 nanospheres, modification with bimetallic PtAu NPs was more effective in enhancing the gas-sensitive efficiency of SnO_2 nanospheres, and their response value was 20.8 times that of pure SnO_2 nanospheres. This improved gas sensitivity was because of the chemical sensitization of the Au NPs, the electron sensitization of Pt NPs, along with the combined impact of bimetallic. The sensor developed in this study can accurately detect ppb-level acetone gas to meet the needs of the diagnosis and early screening of diabetes. Therefore, $PtAu/SnO_2$ nanosphere sensors have considerable potential for the early diagnosis and screening of diabetes.

Supplementary Materials: The following supporting information can be downloaded at: https://www.mdpi.com/article/10.3390/nano14131097/s1, Figure S1: operating parameters of ICP-MS; Figure S2: sensing response of the $PtAu/SnO_2$ sensors to 1 ppm acetone at 300 °C; Table S1: Operating parameters of ICP-MS; Equation (S1); Equation (S2). Ref. [10] is cited in the supplementary materials.

Author Contributions: Conceptualization, X.Z. and R.G.; formal analysis, R.G. and P.C.; investigation, X.Z. and R.G.; writing—original draft preparation, R.G.; writing—review and editing, X.Z., R.G., and H.Y.; visualization, P.C. and Y.Y.; supervision, Y.L.; projection administration, P.L. and Y.L.; funding acquisition, R.G. All authors have read and agreed to the published version of the manuscript.

Data Availability Statement: Data are contained within the article and Supplementary Materials.

Conflicts of Interest: The authors declare no conflicts of interest.

References

1. Zhao, J.; Shen, W.; Lv, D.; Yin, J.; Liang, T.; Song, W. Gas-sensing technology for human breath detection. *Prog. Chem.* **2023**, *35*, 302–317.
2. Lee, S.; Choi, S.; Park, S.H.; Cho, S.H.; Sohn, W.; Eom, T.H.; Kim, Y.; Jang, H.W. Synthesis-in-place hydrothermal growth of hematite nanorods on patterned substrate for highly sensitive and rapid acetone detection. *Sens. Actuators B Chem.* **2023**, *395*, 134519. [CrossRef]
3. Alizadeh, N.; Jamalabadi, H.; Tavoli, F. Breath acetone sensors as non-invasive health monitoring systems: A Review. *IEEE Sens. J.* **2020**, *20*, 5–31. [CrossRef]

4. Feng, G.; Che, Y.; Wang, S.; Wang, S.; Hu, J.; Xiao, J.; Song, C.; Jiang, L. Sensitivity enhancement of In_2O_3/ZrO_2 composite based acetone gas sensor: A promising collaborative approach of ZrO_2 as the heterojunction and dopant for in-situ grown octahedron–like particles. *Sens. Actuators B Chem.* **2022**, *367*, 132087. [CrossRef]

5. Ma, S.; Xu, J. Nanostructured metal oxide heterojunctions for chemiresistive gas sensors. *J. Mater. Chem. A* **2023**, *11*, 23742. [CrossRef]

6. Li, F.; Jing, J.; Li, J.; Li, S.; Ye, S.; Song, X.; Zhan, Z.; Zhang, Y. Fabrication of ZnO–SnO_2 heterojunction inverse opal photonic balls for chemiresistive acetone sensing. *Sens. Actuators B Chem.* **2024**, *400*, 134887. [CrossRef]

7. Mondal, B.; Gogoi, P.K. Nanoscale heterostructured materials based on metal oxides for a chemiresistive gas sensor. *ACS Appl. Electron. Mater.* **2022**, *4*, 59–86. [CrossRef]

8. Walker, J.; Karnati, P.; Akbar, S.A.; Morris, P.A. Selectivity mechanisms in resistive–type metal oxide heterostructural gas sensors. *Sens. Actuators B Chem.* **2022**, *355*, 131242. [CrossRef]

9. Kong, L.; Yuan, Z.; Gao, H.; Meng, F. Recent progress of gas sensors based on metal oxide composites derived from bimetallic metal-organic frameworks. *TrAC Trends Anal. Chem.* **2023**, *166*, 117199. [CrossRef]

10. Zhang, X.; Sun, J.; Tang, K.; Wang, H.; Chen, T.; Jiang, K.; Zhou, T.; Quan, H.; Guo, R. Ultralow detection limit and ultrafast response/recovery of the H_2 gas sensor based on Pd–doped rGO/ZnO–SnO_2 from hydrothermal synthesis. *Microsyst. Nanoeng.* **2022**, *8*, 67. [CrossRef]

11. Xiang, C.; Chen, T.; Zhao, Y.; Sun, J.; Jiang, K.; Li, Y.; Zhu, X.; Zhang, X.; Zhang, N.; Guo, R. Facile hydrothermal synthesis of SnO_2 nanoflowers for low–concentration formaldehyde detection. *Nanomaterials* **2022**, *12*, 2133. [CrossRef] [PubMed]

12. Masuda, Y. Recent advances in SnO_2 nanostructure based gas sensors. *Sens. Actuators B Chem.* **2022**, *364*, 131876. [CrossRef]

13. Zhu, L.; Ou, L.; Mao, L.; Wu, X.; Liu, Y.; Lu, H. Advances in noble metal-decorated metal oxide nanomaterials for chemiresistive gas sensors: Overview. *Nano-Micro Lett.* **2023**, *15*, 89. [CrossRef] [PubMed]

14. Verma, M.; Bahuguna, G.; Singh, S.; Kumari, A.; Ghosh, D.; Haick, H.; Gupta, R. Porous SnO_2 nanosheets for room temperature ammonia sensing in extreme humidity. *Mater. Horiz.* **2024**, *11*, 184. [CrossRef] [PubMed]

15. Pandey, G.; Bhardwaj, M.; Kumar, S.; Lawaniya, S.D.; Kumar, M.; Dwivedi, P.K.; Awasthi, K. Synergistic effects of Pd–Ag decoration on SnO/SnO_2 nanosheets for enhanced hydrogen sensing. *Sens. Actuators B Chem.* **2024**, *402*, 135062. [CrossRef]

16. Lei, B.; Zhang, H.; Liu, W.; Zhao, Q.; Wei, Y.; Lu, Y.; Yang, X.; Zhang, W.; Xiao, T.; Kong, J.; et al. Micro–heater embedded Ni-SnO_2 ordered nanoporous films: On–chip fabrication for fast, sensitive, and selective gas sensing towards multiple VOCs for air quality monitoring. *Sens. Actuators B Chem.* **2024**, *401*, 134907. [CrossRef]

17. Fan, G.; Huo, F.; Guan, J.; Yu, H.; Zhu, Q.; Han, N.; Mo, J.; Chen, Y. MnO_2 enhanced low temperature HCHO sensing performance of SnO_2. *Sens. Actuators B Chem.* **2024**, *412*, 135803. [CrossRef]

18. Li, G.; Cheng, Z.; Xiang, Q.; Yan, L.; Wang, X.; Xu, J. Bimetal PdAu decorated SnO_2 nanosheets based gas sensor with temperature-dependent dual selectivity for detecting formaldehyde and acetone. *Sens. Actuators B Chem.* **2019**, *283*, 590–601. [CrossRef]

19. Zhu, Y.; Meng, X.; Wang, X.; Gao, W. Low detection based on PdPt/In_2O_3 nanospheres for rapid hydrogen detection. *Sens. Actuators B Chem.* **2024**, *410*, 135654. [CrossRef]

20. Luo, N.; Chen, Y.; Zhang, D.; Guo, M.; Xue, Z.; Wang, X.; Cheng, Z.; Xu, J. High–sensitive MEMS hydrogen sulfide sensor made from PdRh bimetal hollow nanoframe decorated metal oxides and sensitization mechanism study. *ACS Appl. Mater. Interfaces* **2020**, *12*, 56203–56215. [CrossRef]

21. Feng, D.; Zhu, Z.; Du, L.; Xing, X.; Wang, C.; Chen, J.; Tian, Y.; Yang, D. Improved sensing performance of WO_3 nanoparticles decorated with Ag and Pt nanoparticles. *Rare Met.* **2021**, *40*, 1642–1650. [CrossRef]

22. Jamnani, S.R.; Moghaddam, H.M.; Leonardi, S.G.; Neri, G.; Ferlazzo, A. VOCs sensing properties of samarium oxide nanorods. *Ceram. Int.* **2024**, *50*, 403–411. [CrossRef]

23. Liang, Z.; Wang, M.; Liu, S.; Hassan, M.; Zhang, X.; Lei, S.; Qiao, G.; Liu, G. One-pot hydrothermal synthesis of self-assembled MoS_2/WS_2 nanoflowers for chemiresistive room-temperature NO_2 sensors. *Sens. Actuators B Chem.* **2024**, *403*, 135215. [CrossRef]

24. Chen, Z.; Liu, W.; Si, X.; Guo, J.; Huo, J.; Zhang, Z.; Cheng, G.; Du, Z. In situ assembly of one–dimensional Pt@ZnO nanofibers driven by a ZIF–8 framework for achieving a high–performance acetone sensor. *Nanoscale* **2023**, *15*, 17206. [CrossRef] [PubMed]

25. Jang, J.S.; Kim, S.J.; Choi, S.J.; Kim, N.H.; Hakim, M.; Rothschild, A.; Kim, I.D. Thin–walled SnO_2 nanotubes functionalized with Pt and Au catalysts via the protein templating route and their selective detection of acetone and hydrogen sulfide molecules. *Nanoscale* **2015**, *7*, 16417. [CrossRef] [PubMed]

26. Wang, Y.; Li, Y.; Yang, L.; Liu, Z.; Li, Y.; Bai, J.; Liu, F.; Liang, X.; Sun, P.; Lu, G. Fast detection of ppm n–pentanol by PtAu alloy nanocrystals decorated flower-like WO_3. *Sens. Actuators B Chem.* **2022**, *371*, 132623. [CrossRef]

27. Chen, K.; Zhou, Y.; Jin, R.; Wang, T.; Liu, F.; Wang, C.; Yan, X.; Sun, P.; Lu, G. Gas sensor based on cobalt–doped 3D inverse opal SnO_2 for air quality monitoring. *Sens. Actuators B Chem.* **2022**, *350*, 130807. [CrossRef]

28. Kim, K.; Choi, P.G.; Itoh, T.; Masuda, Y. Catalyst–free highly sensitive SnO_2 nanosheet gas sensors for parts per billion–level detection of acetone. *ACS Appl. Mater. Interfaces* **2020**, *12*, 51637–51644. [CrossRef]

29. Chen, Y.; Cao, Y. Ultrasensitive and low detection limit of acetone gas sensor based on ZnO/SnO_2 thick films. *RSC Adv.* **2020**, *10*, 35958. [CrossRef]

30. Wang, W.; Xian, J.; Li, J.; Yu, M.; Duan, Q.; Leung, C.M.; Zeng, M.; Gao, X. Construction of Co_3O_4/SnO_2 yolk–shell nanofibers for acetone gas detection. *Sens. Actuators B Chem.* **2024**, *398*, 134724. [CrossRef]

31. Guo, W.; Luo, R.; Liu, F.; Wang, X. Enhanced acetone gas sensing performance of Zn_2SnO_4/SnO_2 hierarchical stack structure. *Mater. Lett.* **2023**, *352*, 135176. [CrossRef]

32. Bai, J.; Wang, C.; Liu, K.; Wang, H.; Liu, Y.; Liu, F.; Suo, H.; Liang, X.; Zhang, C.; Liu, F.; et al. Ehnahced gas sensing performance based on the PtCu octahedral alloy nanocrystals decorated SnO_2 nanoclusters. *Sens. Actuators B Chem.* **2021**, *330*, 129375. [CrossRef]

33. Shao, S.; Chen, X.; Chen, Y.; Lai, M.; Che, L. Ultrasensitive and highly selective detection of acetone based on Au@WO_3–SnO_2 corrugated nanofibers. *Appl. Surf. Sci.* **2019**, *473*, 902–911. [CrossRef]

34. Jeong, Y.J.; Koo, W.T.; Jang, J.S.; Kim, D.H.; Cho, H.J.; Kim, I.D. Chitosan–templated Pt nanocatalyst loaded mesoporous SnO_2 nanofibers: A superior chemiresistor toward acetone molecules. *Nanoscale* **2018**, *10*, 13713. [CrossRef]

35. Sui, N.; Wei, X.; Cao, S.; Zhang, P.; Zhou, T.; Zhang, T. Nanoscale bimetallic AuPt–functionalized metal oxide chemiresistors: Ppb–level and selective detection for ozone and acetone. *ACS Sens.* **2022**, *7*, 2178–2187. [CrossRef]